ELSEVIER

Earth and Planetary Science Letters 202 (2002) 725–740

EPSL

www.elsevier.com/locate/epsl

A continuum mechanics model for normal faulting using a strain-rate softening rheology: implications for thermal and rheological controls on continental and oceanic rifting

Mark D. Behn [a,*], Jian Lin [b], Maria T. Zuber [c]

[a] *MIT/WHOI Joint Program, Woods Hole Oceanographic Instituion, Woods Hole, MA 02543, USA*
[b] *Department of Geology and Geophysics, Woods Hole Oceanographic Instituion, Woods Hole, MA 02543, USA*
[c] *Massachusetts Institute of Technology, Cambridge, MA 02139, USA*

Received 18 October 2001; received in revised form 24 June 2002; accepted 27 June 2002

Abstract

We use a strain-rate-dependent visco-plastic rheology in a finite element model to investigate the effects of crustal rheology and thermal structure on the development of normal faults in 2-D extending lithosphere. Strain-rate softening in the brittle regime is used to simulate the rate-dependence of frictional strength observed in laboratory studies. Results of numerical experiments show that efficient strain-rate softening can result in localized zones of high strain rate, which develop in response to the rheology and boundary conditions and are not imposed a priori. We argue that these zones of localized shearing are analogous to faults and use the calculated deformation field to predict the preferred location of fault formation for a range of thermal and rheologic conditions. When no regional temperature gradient is imposed, deformation is predicted to be distributed between several sets of conjugate normal faults. However, in the presence of a horizontally varying temperature field, faulting is calculated to focus where the lithosphere is thinnest, forming rift-like topography. Model results predict that when crustal thickness is sufficiently small that no ductile layer is present in the lower crust, deformation is *mantle-dominated* and rift half-width is controlled primarily by the vertical geothermal gradient. In contrast, when crustal thickness is large enough that the stress accumulation in the upper crust becomes much greater than the stress accumulation in the upper mantle, deformation becomes *crust-dominated* and the calculated rift half-width is a function of both crustal rheology and the vertical geothermal gradient. This implies that deformation in the brittle upper crust does not behave independently of a strong upper mantle, even in situations where ductile flow occurs in the lower crust.

Keywords: rheology; lithosphere; deformation; strain; rifting

1. Introduction

Rift zones are areas of localized lithospheric extension, typically characterized by a central basin bounded on either side by inward dipping normal faults. Rift flanks are generally uplifted, and

* Corresponding author. Tel.: +1-508-289-3490; Fax: +1-508-457-2150.
E-mail addresses: mbehn@whoi.edu (M.D. Behn), jlin@whoi.edu (J. Lin), zuber@mit.edu (M.T. Zuber).

0012-821X/02/$ – see front matter
PII: S0012-821X(02)00792-6

the lithosphere beneath a rift zone is often abnormally thin. Extensional environments are commonly associated with regional uplift, high heat flow, and local magmatism, indicating the presence of a thermal anomaly. Rift zones are observed in both continental (e.g., Rio Grande Rift, Rhine Graben) and oceanic lithosphere (e.g., mid-ocean ridges), and represent the initial stage of continental breakup and seafloor spreading. In this study, we investigate the relationship between the development of rift systems and the rheologic properties of the lithosphere.

The rheologic structure of the lithosphere is often assumed to consist of a brittle layer overlying a ductile region at depth [1,2]. In the brittle regime, strain is accommodated on faults when stress exceeds the frictional resistance on a fault plane. Friction on rock surfaces has been shown to be a complex non-linear function of overburden pressure [3], strain and loading history [4,5], and sliding velocity [6,7]. In the ductile regime, strain is controlled by a temperature-dependent power law that relates stress and strain-rate [8]. Using these relationships, experimentally derived friction and flow laws for crustal and mantle rocks can be incorporated into numerical models of rifting in order to improve our understanding of the tectonic processes that create rift morphology.

A common formulation for the development of normal faults in extensional environments is to treat the lithosphere as an elastic layer floating on an inviscid fluid (e.g., [9–14]). Normal faults are assumed to penetrate the lithosphere, with displacement on an individual fault accumulating until the shear stresses exceed the brittle strength of the lithosphere and a new fault is formed. Unfortunately, these models generally require that the location and dip of faults be specified a priori [15–18], rather than developing in response to the evolving stress field. An alternative class of models assumes that the lithosphere behaves as a non-Newtonian viscous fluid. This approach has been used to describe rift morphology [19–21], the characteristic spacing of faults [22,23], and dynamic topography [24] in extensional environments. An assumption of these continuum models is that deformation occurs on closely spaced faults that can be approximated by plastic flow.

A third approach that has been used to simulate deformation in extensional environments couples an elasto-plastic rheology in the brittle portion of the lithosphere with an elasto-viscous rheology at depth [25–28]. Several recent studies have used this elasto-visco-plastic approach to examine the interaction between non-linear frictional resistance laws and non-Newtonian viscous flow laws. Poliakov and Buck [29] simulated cohesion loss on a fault surface by including strain softening in models of abyssal hill formation at mid-ocean ridges. Similarly, Lavier et al. [30] used cohesion loss to model the development of low angle normal faults in continental environments. Using a different approach, Frederiksen and Braun [31] illustrated that strain softening in the ductile regime could lead to strain localization and the development of mantle shear zones during lithospheric extension. However, these studies do not include the strain-rate dependence of frictional strength on a fault surface that is observed in laboratory studies.

In this study, we incorporate strain-rate softening into the brittle regime of a visco-plastic model of lithospheric stretching. Localized deformation corresponds to zones of high strain rate that develop in response to the rheology and boundary conditions, and are not imposed a priori. Using this formulation, we test the sensitivity of the predicted pattern of deformation to crustal thickness, thermal structure, and the rheologic flow laws describing the crust and mantle. Finally, we compare the results of our numerical simulations to natural examples of continental and oceanic rifts and discuss the implications for the development and evolution of extensional systems.

2. Model setup

At high temperatures geologic materials are observed to flow by dislocation creep, which results in a non-Newtonian power law rheology [2,8]

$$\dot{\varepsilon} = A(\sigma_1 - \sigma_3)^n \exp(-Q/RT) \quad (1)$$

where $\dot{\varepsilon}$ is the uniaxial strain rate, σ_1 and σ_3 are the maximum and minimum principle stresses, n is the power law exponent, Q is the molar activation energy, A is a material strength constant, T is the temperature, and R is the gas constant (see Table 1 for list of model parameters). The material parameters (A, n, Q) can be determined from laboratory experiments (e.g., [32]) and are approximately independent of stress and temperature. Although the relationship between stress and strain rate is non-linear, we can define a linearized viscosity law [24] by

$$\tau_{ij} = \sqrt{2}\eta\dot{\varepsilon}_{ij} \tag{2}$$

where τ_{ij} is the stress tensor, η is the effective viscosity, and $\dot{\varepsilon}_{ij}$ is the strain-rate tensor. This linearization leads to an expression for the apparent effective Newtonian viscosity

$$\eta = B\dot{\varepsilon}_{\mathrm{II}}^{(1-n)/n}\exp(Q/nRT) \tag{3}$$

where $\dot{\varepsilon}_{\mathrm{II}}$ is the second invariant of the stain rate tensor, and

$$B = \frac{1}{4}\left(\frac{4}{3A}\right)^{1/n} \tag{4}$$

In the brittle regime, strength is often assumed to be controlled by a frictional resistance law (e.g., [3,33])

$$\tau_{\max} = \sigma_o - C\sigma_n \tag{5}$$

where σ_o is the cohesive strength, C is the Coulomb strength coefficient, and σ_n is approximately equal to the lithostatic stress. C is defined by

$$C = \frac{\sin(\theta)}{1+\sin(\theta)} \tag{6}$$

where θ is the angle of internal friction, which is in turn related to the coefficient of friction, μ, by $\mu = \tan(\theta)$ [34]. Thus for typical values of μ between 0.6 and 0.85, $C = 0.34$–0.39. Laboratory experiments have shown that dynamic friction is a

Table 1
Model parameters

	Definition	Value	Units
g	gravitational acceleration	9.8	m s^{-2}
R	universal gas constant	8.3144	J mol^{-1} K^{-1}
T	temperature		K
n_c, n_m	power law exponent (crust, mantle)		
A_c, A_m	material strength constant (crust, mantle)		MPa^{-n} s^{-2}
Q_c, Q_m	molar activation energy (crust, mantle)		J mol^{-1}
$\dot{\varepsilon}_o$	reference strain rate	10^{-14}	s^{-1}
$\dot{\varepsilon}_{\mathrm{II}}$	second invariant of the strain rate tensor		s^{-1}
η	effective viscosity		Pa s
ρ_c, ρ_m	density (crust, mantle)	2700, 3300	kg m^{-3}
C	Coulomb strength coefficient		
C_o	reference Coulomb strength coefficient		
θ	angle of internal friction		
μ	reference coefficient of friction		
σ_o	cohesive strength	50	MPa
σ_n	lithostatic stress		MPa
γ	strain-rate softening coefficient		
t_c	crustal thickness		km
x, z	horizontal and vertical coordinates		km
X_o, Z_o	horizontal and vertical dimensions of model space		km
u_x, u_z	horizontal and vertical velocities		m s^{-1}
z_o	depth to 700°C isotherm at $x = 0$		km
$d\bar{z}/dx$	slope of the 700°C isotherm		
$\frac{\partial T}{\partial z}(x)$	vertical geothermal gradient		K/km

function of the sliding velocity, with fault surfaces experiencing lower coefficients of friction at higher strain rates (e.g., [6,7,35]). The degree of strain-rate softening is roughly proportional to the logarithm of the sliding velocity over several orders of magnitude [33]. Furthermore, laboratory studies have also shown static friction on fault surfaces exhibits time-dependent behavior, with the coefficient of friction increasing logarithmically with hold time [36–38]. To simulate the observed time-dependence of frictional strength, we follow the formulation of Neumann and Zuber [39] and Montési et al. [40], expressing the apparent Coulomb strength coefficient, C, as

$$C = C_o(1-\gamma\log_{10}(\dot{\varepsilon}_{\mathrm{II}}/\dot{\varepsilon}_{\mathrm{o}})) \quad (7)$$

where C_{o} is the reference strength coefficient, γ is the strain-rate softening coefficient, and $\dot{\varepsilon}_{\mathrm{o}}$ is the reference strain rate. Note that this frictional law is an implicit function of the grid size, with coarser grids resulting in smaller values of $\dot{\varepsilon}_{\mathrm{II}}$ in a heterogeneously deforming grid mesh. The importance of this effect will be discussed in Section 3.1.

2.1. Numerical procedure

Following the numerical approach of Neumann and Zuber [39], we use a Lagrangian visco-plastic finite element model to calculate extension in a 2-D vertical cross-section of lithosphere. The model space is discretized into 4-node quadrilateral elements, in which the forces applied to each element, f^{e}, are linearly related to the velocities, u^{e}, through the element stiffness matrix, K^{e}. The penalty method with reduced integration [41] is used to define the element stiffness matrices, which are then assembled to form the global stiffness matrix, K. After imposition of the natural (force) and essential (velocity) boundary conditions, the global system of equations, $Ku=f$, is solved for the incompressible flow field throughout the model space. The non-linear rheology described above can be solved by iterative linearization of the effective viscosity in each finite element as follows (see also [23,24]):

1. Calculate the initial effective viscosity for each element from Eq. 3 based on the prescribed temperature field, $T(x,z)$, and a uniform reference strain rate, $\dot{\varepsilon}_{\mathrm{o}}$.
2. For elements in which the resulting maximum principle shear stress, $\tau_{ij} = \sqrt{2}\eta\dot{\varepsilon}_{\mathrm{II}}$, is greater than the frictional failure criterion, $\tau_{\max}$, reset the effective viscosity of the element to $\eta = \tau_{\max}/\sqrt{2}\dot{\varepsilon}_{\mathrm{II}}$.
3. Form global stiffness matrix, K, prescribe velocity boundary conditions and gravitational body forces, and solve the finite element equation, $Ku=f$, for the velocities u.
4. Based on the velocities calculated in Step 3, recalculate the strain rate in each element and use Eq. 3 to update the element effective viscosities.
5. Repeat steps 2–4 until the desired level of convergence is reached.
6. Deform grid by applying nodal velocities, u, over a reference time step Δt.
7. Repeat steps 2–6 until 1% total strain is achieved.

The results of the numerical experiments presented here should be treated as a proxy for the initial pattern of deformation that will develop for a given set of thermal and rheologic parameters, rather than as a method to study the evolution of individual faults over geologic time. The rotation of fault blocks in highly extended terrains can generate large flexural stresses (e.g., [11,12]) that are not accounted for in the visco-plastic formulation described above. By limiting our numerical experiments to a maximum of 1% total extension, we can safely ignore these elastic stresses and also eliminate numerical inaccuracies associated with the distortion of model elements.

The numerical model setup is illustrated in Fig. 1. A uniform horizontal velocity, $u_x = U$, is imposed on the right-hand side of the model space ($x = X_{\mathrm{o}}$). For numerical efficiency, a symmetry condition is placed on the left-hand side of the model ($x = 0$) such that $u_x = 0$ and $\tau_{xz} = 0$. The top boundary ($z = 0$) is stress free. Because we consider only small far-field strains, hydrostatic restoring forces associated with lithospheric and crustal thinning will be small and we assume the bottom boundary ($z = Z_{\mathrm{o}}$) is free-slip with no vertical velocity. The model dimensions, $X_{\mathrm{o}} = 55$ km and $Z_{\mathrm{o}} = 60$ km, are specified to insure that the

boundaries do not significantly influence the final solution. For each numerical experiment the finite element grid is adjusted to give maximum resolution (with grid size of 300×300 m) where strain is concentrated. The crustal thickness, t_c, is defined to be constant across the model space, with the crust and mantle material parameters given by A_c, n_c, Q_c and A_m, n_m, Q_m, respectively. The reference strain rate, $\dot{\varepsilon}$, is defined to be 10^{-14} s^{-1}, and the strain rates reported here are referenced to this value.

The temperature field is defined by two parameters, the depth to the 700°C isotherm at $x=0$, $\bar{z}_o$, and the slope of the 700°C isotherm, $d\bar{z}/dx$ (Fig. 1). Above the 700°C isotherm, temperature is assumed to be controlled by conductive cooling and is linear with depth,

$$T(x, z \leq \bar{z}) z = \frac{\partial T}{\partial z}(x) \tag{8}$$

For depths greater than $\bar{z}$, temperature follows a steady-state half-space cooling model,

$$T(x, z > \bar{z}) =$$

$$700 + (T_m - 700)\mathrm{erf}\left(\frac{\sqrt{\pi} z}{2(T_m - 700)} \frac{\partial T}{\partial z}(x)\right) \tag{9}$$

where T_m is the mantle temperature and $\frac{\partial T}{\partial z}(x)$ is the vertical geothermal gradient defined by $\bar{z}_o$ and $d\bar{z}/dx$ at all points across the model space.

3. Numerical results

In this section we present a series of numerical experiments to evaluate the sensitivity of the predicted style of lithospheric deformation to the degree of strain-rate softening, regional thermal structure, crustal thickness, and the rheologic flow laws used to describe the crust and mantle.

3.1. Strain-rate softening coefficient

In order to examine the effect of strain-rate softening on the pattern of deformation during extension, we tested a range of values for the strain-rate softening coefficient, γ, between 0 and 0.2. Fig. 2a,b shows the deformed finite element grid for γ values of 0 and 0.15, respectively. When strain-rate softening is ignored ($\gamma=0$), a diffuse region of moderately high strain-rates develops near the rift axis. In contrast, when $\gamma=0.15$, high strain rates are focused into a narrow zone of localized deformation, resulting in a fault-like scarp in the surface topography (Fig. 2c). In both cases the predicted pattern of strain is more developed at some distance away from the rift axis. This is caused by the formation of a plastic shear zone (either diffuse or localized) in response to the thermal perturbation and the downward motion of material above this zone as a block. Note that the topography resulting from purely visco-plastic deformation results in very little uplift of the rift flanks, consistent with results from previous numerical studies [28,42].

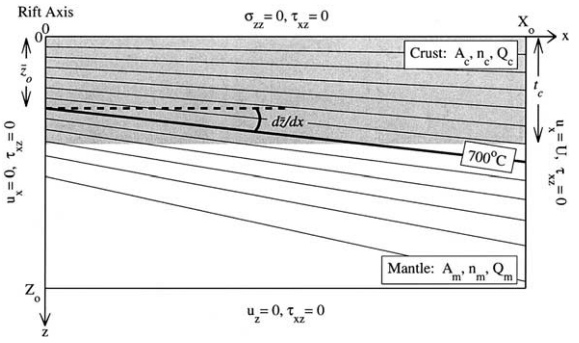

Fig. 1. Model setup for numerical simulations of lithospheric stretching. The model space is symmetric about the rifting axis ($x=0$), with dimensions X_o and Z_o. A uniform horizontal velocity, $u_x=U$ is applied to the right-hand side of the model space, and extension is continued until 1% total strain is achieved. Crustal thickness, t_c, is constant across the model space, with the crust and mantle rheological parameters given by A_c, n_c, Q_c and A_m, n_m, Q_m, respectively. The temperature field is described by the depth to the 700°C isotherm at the rift axis, $\bar{z}_o$, and the slope of the 700°C isotherm, $d\bar{z}/dx$.

Fig. 3a illustrates the degree to which the strain-rate softening coefficient controls both the calculated width of the deformation zone and the maximum value of strain rate at $z=0$ km. The minimum width of the deformation zone is controlled by the spacing of the finite element grid, and is ~4 elements wide. Based on this analysis, it appears that values of $\gamma \geq 0.10$ are sufficient to

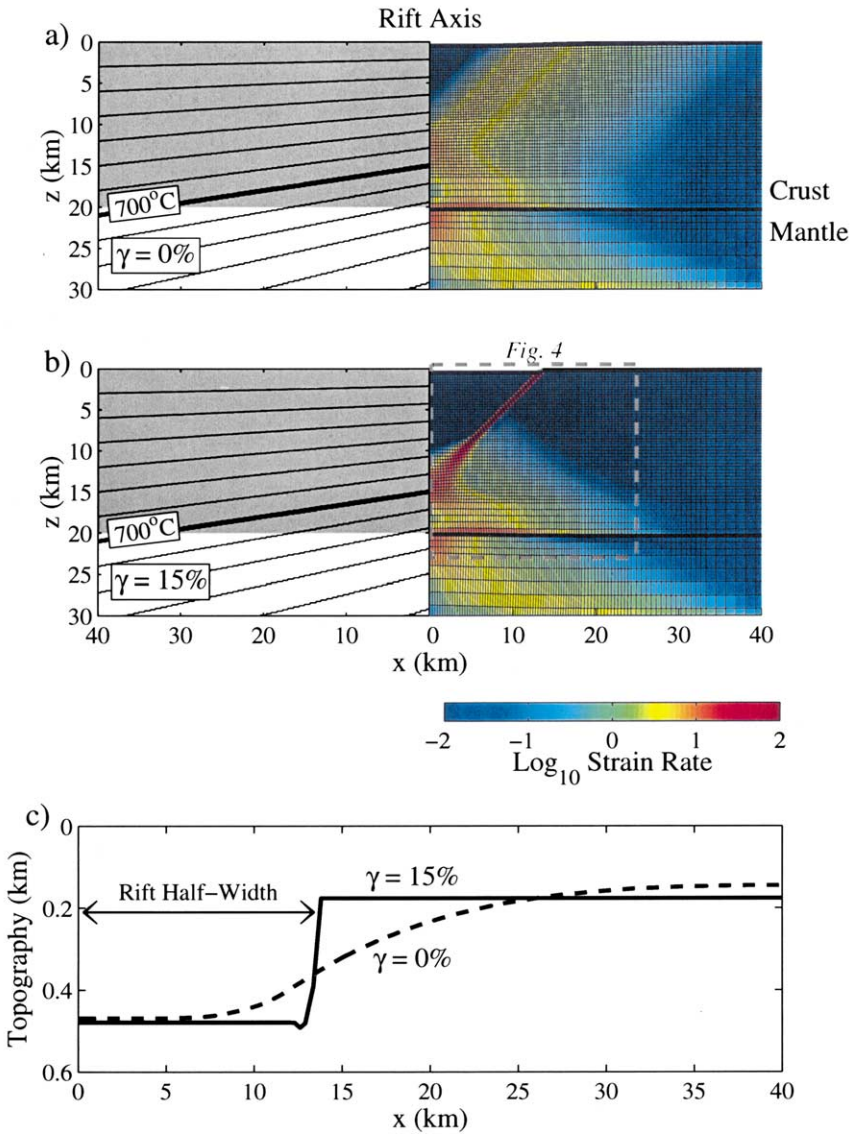

Fig. 2. Numerical simulations illustrating the importance of the strain-rate softening coefficient, γ, on localizing deformation into narrow fault-like shear zones. (a) $\gamma = 0$. (b) $\gamma = 0.15$. The deformed finite element grid (right) is shown after 1% total strain, with colors representing the second invariant of the strain-rate tensor normalized to the reference strain-rate, $\dot{\varepsilon}_o$, in each element. Only upper left portion of model is shown; overall model dimensions are $X_o = 55$ km and $Z_o = 60$ km. The initial temperature field ($\bar{z} >_o = 15$ km, $d\bar{z}/dx = 0.15$) is shown on the left, with temperature contour interval of 100°C. A 20-km-thick crust is assumed (gray box on left; bold lines on right). The experimental flow laws 3 [51] and 7 [32] from are used for the crust and mantle, respectively. Location of Fig. 4 is shown by dashed box. (c) Surface topography of numerical simulations in (a) and (b). Note that the incorporation of strain-rate softening focuses high strain rates into a narrow zone, generating a fault-like scarp in the surface topography.

localize deformation in a narrow shear zone analogous to a fault (refered to hereafter as a 'fault zone'), and we choose $\gamma = 0.15$ for the remainder of the numerical experiments presented in this study. For the ~ 2 order of magnitude increase in $\dot{\varepsilon}_{II}$ relative to $\dot{\varepsilon}_o$ within the fault zone shown in Fig. 2b, $\gamma = 0.15$ would result in a $\sim 30\%$ reduction of the apparent strength coefficient, C, and a $\sim 50\%$ reduction in the coefficient of friction, μ.

Values of γ derived from laboratory experiments range from 0.01 to 0.025 [37,38], approximately one order of magnitude lower than the values necessary for localization in our numerical experiments. The reason for this discrepancy is likely related to the difficulties in scaling laboratory-based friction laws to lithospheric-scale models of deformation. For example, as noted earlier, the grid spacing of the numerical model can influence the average strain rate in each element and thus the degree of localization for a given γ value (Eq. 7). If the grid resolution is increased, a smaller value of γ will be required to generate an equivalent amount of weakening (Fig. 3b). We observe that while the magnitude of the weakening parameter is scale-dependent, the location of the predicted fault zone is not significantly affected by the chosen grid resolution.

It is important to note that the predicted pattern of deformation develops in response to the initial temperature field, crustal thickness, and rheologic flow laws, and is not imposed a priori. Thus, the results of our numerical simulations can be used to predict the preferred location of fault formation for an initial set of thermal and rheologic conditions. Neumann and Zuber [39] also used a strain-rate softening rheology in the brittle regime to model the development of fault-like shear zones in an extending lithosphere. However, they considered only a horizontally homogeneous plate exposed to a 0.5-km perturbation in surface topography at the rift axis. In the models presented here, the initial topography of the model space is uniform, and the deformation pattern develops from the prescribed horizontal variations in the temperature field.

Fig. 4 shows the stress field around the fault zone in Fig. 2b. The effective viscosity of the elements within the fault zone is typically four to six

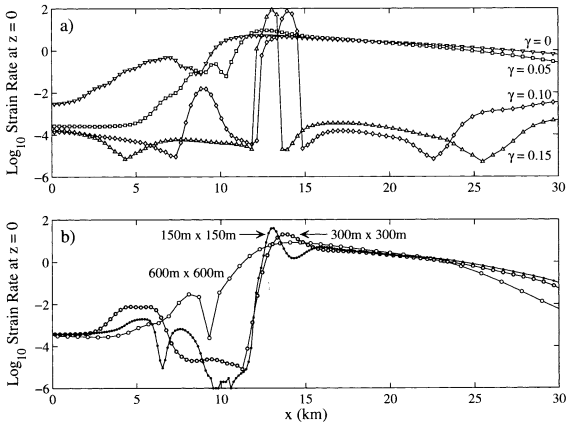

Fig. 3. (a) Comparison of the calculated strain-rate at $z = 0$ km for γ values of 0, 0.05, 0.10 and 0.15, and a grid resolution of 300×300 m. Larger values of γ result in a narrower deformation zone and a higher maximum strain-rate within the zone. Values of $\gamma \geq 0.10$ are sufficient to localize deformation into a narrow region analogous to a fault zone. Variations in strain-rate with magnitudes $< 10^{-3}$ s^{-1} are numerical effects and do not impact the final model solutions. (b) Effect of grid resolution on the predicted localization in the brittle layer with $\gamma = 0.075$. Grid spacings are 150×150 m (black dots), 300×300 m (gray circles), and 600×600 m (white circles). Localization is enhanced with increasing grid resolution. However once a narrow shear zone forms, its location is not overly sensitive to the grid resolution and γ used.

orders of magnitude lower than in the adjacent regions. High stresses ($\tau_{max} > 100$ MPa) are predicted near the base of the brittle upper crust and in the upper mantle, while the ductile lower crust is characterized by values of $\tau_{max} < 20$ MPa. Within the fault zone, stresses are also low due to the low effective viscosity of these elements. This is significant because it implies that our visco-plastic formulation for strain-rate softening is limited to generating 'weak' faults characterized by low friction coefficients. The physical implication of this limitation is that the fault zones formed in our models will be characterized by dip angles of 45°. The zones adjacent to the fault, however, are characterized by elevated stresses. In the foot wall, the direction of maximum tensile stress is rotated from horizontal into the direction of deformation. This prediction is similar to modeling by Chéry [18] of the stress field around a weak fault zone in a visco-elastic space.

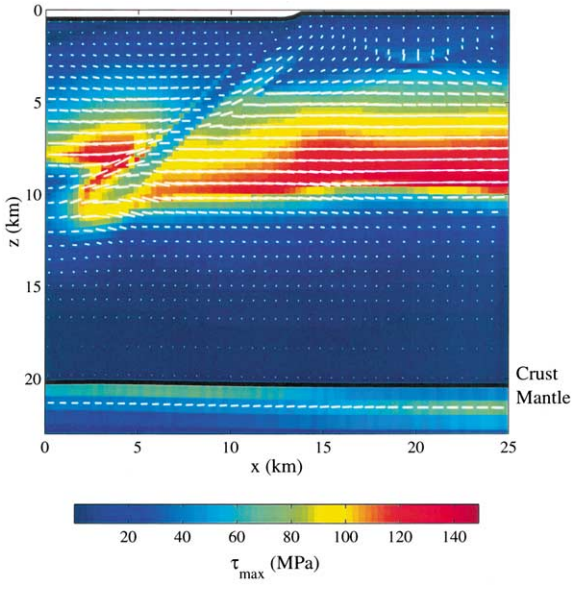

Fig. 4. Stress field corresponding to the numerical simulation shown in Fig. 2b. Colors indicate the magnitude of τ_{max} in each element and white lines show the direction of maximum tensile stress with length scaled to the magnitude of τ_{max}. Thick black line represents crust–mantle boundary. Note that τ_{max} reaches a maximum value near the base of the brittle upper crust and increases again in the upper mantle. Note also that the region of high strain rate in the inclined 'fault-like' shear band corresponds to an area of rotated maximum tensile stress direction and a decrease in the magnitude of τ_{max}.

3.2. Horizontal temperature gradient

Extension in continental lithosphere typically results in the formation of either wide (e.g., basin and range) or narrow (e.g., Rhine Graben, Baikal) rift zones. Models to distinguish between these two styles of rifting have focused on the thermal evolution of the lithosphere through time. In these models thermal state is the result of equilibrium between the relative rates of heat advection due to athenospheric upwelling and thermal diffusion through increased surface heat flow (e.g., [43,44]). Narrow rift zones are thought to result from runaway lithospheric thinning caused by rapid extension, while wide rifts develop when strain rates are low and thermal diffusion dominates [45]. Other mechanisms that have been proposed to produce wide rifts include viscous strengthening and isostatic compensation of rift-related topography [46]. Because our numerical experiments are limited to small amounts of total strain, we cannot examine the long-term evolution of rift zones in which thermal state may evolve as a function of necking, viscous

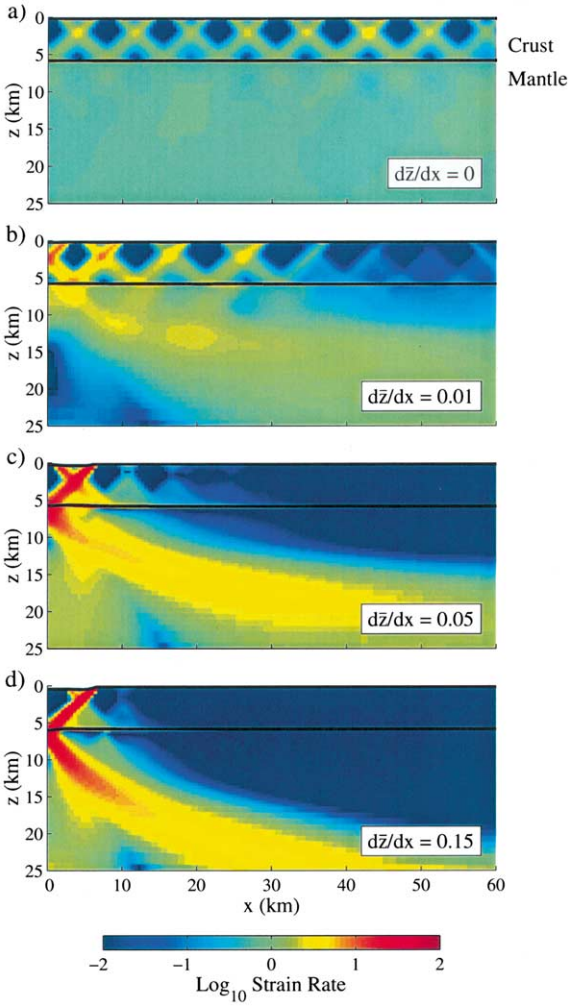

Fig. 5. Numerical simulations illustrating the importance of the horizontal temperature gradient in localizing deformation on a regional scale. (a–d) show deformed finite element grids after 1% total strain for $\bar{z}_o = 5$ *km and* $d\bar{z}/dx = 0$, 0.01, 0.05 and 0.15, respectively. A 6-km-thick crust is assumed (bold lines), and the flow laws 3 [51] and 7 [32] from Table 2 are used for the crust and mantle, respectively. When no lateral temperature gradient is present (a), deformation is distributed between several sets of conjugate normal faults. However, when $d\bar{z}/dx > 0.10$, deformation is localized on one major fault near the rift axis.

flow, sedimentation and erosion. However, assuming the pattern of deformation will equilibriate rapidly relative to the evolving thermal conditions, we can examine the sensitivity of deformation to the thermal state of the lithosphere.

Fig. 5 illustrates the deformation pattern calculated for four different horizontal temperature gradients. In each numerical experiment, the depth of the 700°C isotherm at the rift axis, $\bar{z}_o$, is held constant at 5 km, while the horizontal slope of the 700°C isotherm, $d\bar{z}/dx$, is varied from 0 to 0.15. We choose a maximum horizontal gradient of 0.15 because it corresponds to the approximate gradient predicted for slow-spreading mid-ocean ridge with a spreading half-rate of 1 cm/yr. When no horizontal gradient is present ($d\bar{z}/dx = 0$), deformation is predicted to be distributed over several sets of conjugate normal faults (Fig. 5a). As the value of $d\bar{z}/dx$ is increased, deformation focuses near the thinnest part of the lithosphere (Fig. 5b,c). This focusing is characterized by fewer predicted faults, higher strain rates on individual faults, and a preferential dip direction toward the rift axis. Values of $d\bar{z}/dx > 0.10$ result in focusing onto a single fault centered near the rift axis (Fig. 5d).

3.3. Crustal thickness

Crustal thickness is also predicted to play an important role in controlling the style of deformation during extension. Crustal rocks are typically weaker than mantle rocks (e.g., [8]). Therefore, under a constant set of thermal conditions the brittle–ductile transition will tend to be shallower in rifts with thick crust than in those with thin crust. We investigated the influence of crustal thickness, t_c, on rift half-width for values of t_c ranging from 0 to 40 km (Fig. 6). Rift half-width is defined as the distance from the rift axis to the topographic scarp formed by the primary fault-like shear zone (see Fig. 2c). For small values of t_c, the entire crustal layer is predicted to behave brittly and the resultant rift half-width is independent of crustal thickness. However, once t_c is large enough for a ductile region to form in the lower crust, rift half-width is calculated to decrease with increasing crustal thickness. Eventually, t_c becomes sufficiently large that rift half-width no longer decreases and remains constant for further increases in t_c.

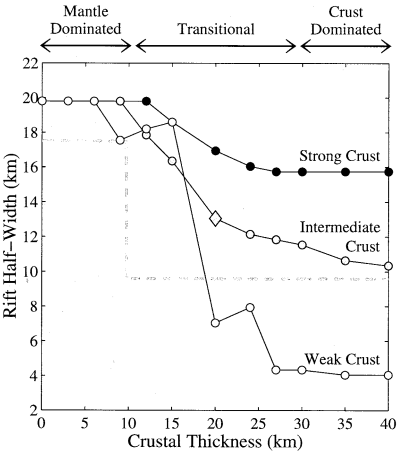

Fig. 6. Effect of crustal thickness on predicted rift half-width. Each dot represents the results of one numerical experiment. The initial temperature field is defined by $\bar{z}_o = 15$ km, $d\bar{z}/dx = 0.15$, resulting in a vertical geothermal gradient of 46 K/km at $x = 0$ km. Calculations were performed using the crustal flow laws for a weak (flow law 2 [50] in Table 2, white circles), intermediate (flow law 3 [51], gray circles), and strong (flow law 6 [52], black circles) rheology. Gray diamond represents model run shown in Fig. 2b. Rift half-width is defined as the distance from the rift axis to the calculated topographic scarp formed by the primary fault zone. All calculations were performed with $d\bar{z}/dx = 0.15$ (see Fig. 2c). The dashed line illustrates the prediction of the analytical solution of Shaw and Lin [14] for flow law 3. Note that the change from mantle- to crust-dominated deformation does not occur at a critical crustal thickness as predicted by Shaw and Lin [14], but rather over a transitional range of crustal thicknesses. The strong rheology results in a rift half-width in the crust-dominated regime that is $\sim$1.5 and $\sim$4 times that predicted by the intermediate and weak rheologies, respectively.

We term the two regimes in which rift half-width is independent of crustal thickness *mantle-dominated* (t_c small, rift half-width large) and *crust-dominated* (t_c large, rift half-width small) deformation, respectively. The range of crustal thicknesses over which deformation changes from mantle-dominated to crust-dominated is refered to as the transition zone (see Fig. 6). Gerbault et al. [47] described a similar transition in compressional systems from faulting in a coupled crust–mantle layer to faulting in only the crustal

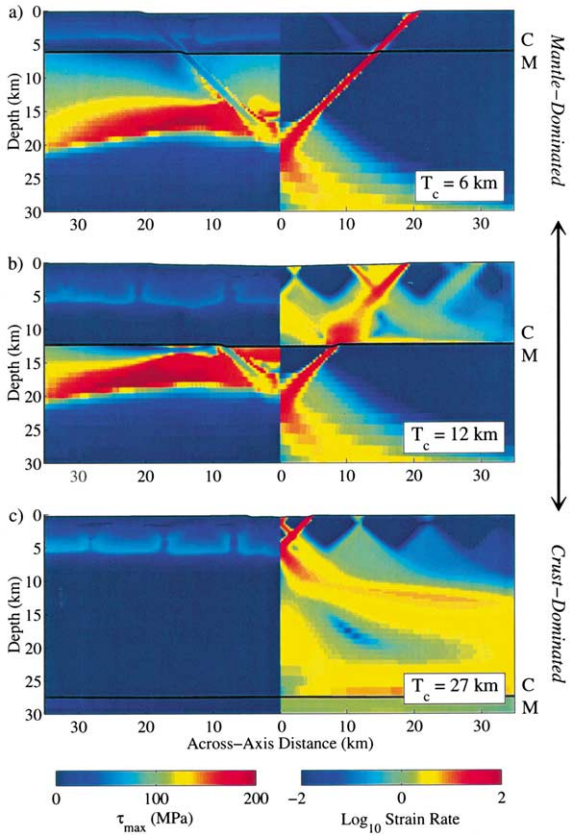

Fig. 7. Numerical simulations illustrating the transition from mantle- to crust-dominated deformation. (a–c) show the deformed finite element grid after 1% total strain for $t_c = 6$, 12 and 27 km, respectively. Colors indicate the magnitude of τ_{max} on left and normalized strain-rate on right. C and M mark the base of the crust and top of the mantle, respectively. The initial temperature field is defined by $\bar{z}_o = 15$ km, $d\bar{z}/dx = 0.15$, resulting in a vertical geothermal gradient of 46 K/km at $x = 0$ km. The experimental flow laws 2 [50] and 7 [32] from Table 2 are used for the crust and mantle, respectively. Note in (b) that deformation in the upper crust is predicted to be coupled to the mantle even when a ductile layer is present in the lower crust.

layer. Fig. 7 shows three numerical experiments illustrating the transition from mantle- to crust-dominated deformation. Note that the transition to crust-dominated deformation is complete only when stress accumulation in the upper crust is much greater than stress accumulation in the upper mantle. The numerical experiments presented in Sections 3.4 and 3.5 allow us to constrain how the transition from mantle- to crust-dominated deformation varies as a function of both crustal rheology and thermal state.

3.4. Crustal rheology

Within the ductile deformation regime, the strength of the crust at a given temperature and strain rate is defined by the material parameters A_c, n_c, and Q_c in Eq. 1. The flow laws for a wide range of crustal and mantle rocks have been determined in experimental studies. In addition to mineralogy (e.g., quartz vs. feldspar aggregates), water content plays an important role in controlling the strength of a material [48]. For example, in samples of diabase the presence of water can result in a two- to three-order of magnitude decrease in effective viscosity [49]. The use of a dry rheology may be particularly relevant in environments that experience volcanism during rifting, as water is an incompatible element and likely to be preferentially extracted during the initial stages of melting. Table 2 lists experimental flow laws for several different wet and dry crustal rheologies, which we classify as weak, intermediate, and strong. Fig. 8 shows the effective viscosity versus depth for these rheologies assuming $\bar{z}_o = 15$ km (or a vertical geothermal gradient of 46 K/km at $x = 0$ km).

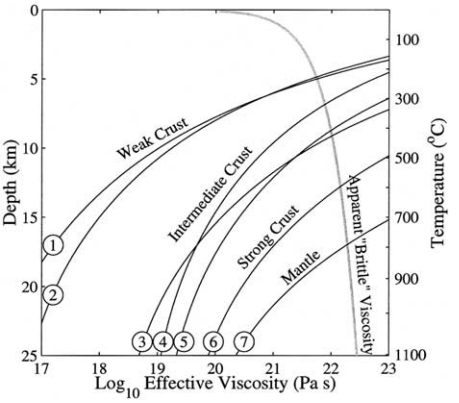

Fig. 8. Effective viscosity as a function of depth for the experimentally determined flow laws given in Table 2. Solid gray line illustrates apparent 'brittle' viscosity calculated from the frictional resistance law in Eq. 5. Temperatures are calculated for $\bar{z}_o = 15$ km, corresponding to a vertical geothermal gradient of 46 K/km. Reference strain-rate of 10^{-14} s^{-1} was used for all calculations.

In Fig. 6 we illustrate the effect of crustal rheology on rift half-width for a weak (flow law 2 [50] in Table 2), intermediate (flow law 3 [51]), and strong (flow law 6 [52]) rheology. All three rheologies predict the same rift half-width in the mantle-dominated deformation regime. However, the transition between mantle- and crust-dominated deformation is predicted to begin at a slightly larger crustal thickness for the strong rheology than for the intermediate or weak rheologies. Further, the strong rheology results in a rift half-width for the crust-dominated regime that is ~1.5 times greater than the value predicted by the intermediate rheology and ~4 times greater than that predicted by the weak rheology. In reality, the lower continental crust is most likely composed of a feldspar-dominated mineralogy [53]. Thus, model results corresponding to either the strong or intermediate rheologies are most applicable to continental extensional environments.

3.5. Vertical geothermal gradient

In Section 3.2, horizontal variations in temperature were shown to play an important role in localizing deformation on a regional scale. Here we illustrate how the vertical geothermal gradient, $\frac{\partial T}{\partial z}(x)$, affects rift half-width for values of $\frac{\partial \bar{T}}{\partial z}(x=0)$ ranging from 25 to 140 K/km (Fig. 9). Our numerical results predict that as the vertical geothermal gradient decreases, rift half-width increases. Moreover, smaller geothermal gradients also result in larger changes in the predicted rift

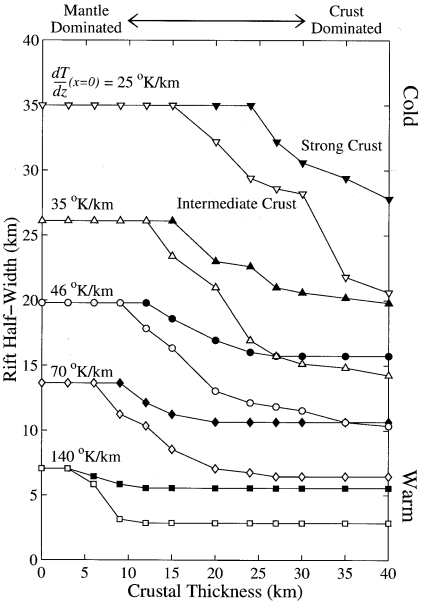

Fig. 9. Effect of the vertical geothermal gradient on the predicted rift half-width. Geothermal gradients of 140 (squares), 70 (diamonds), 46 (circles), 35 (triangles) and 25 K/km (inverted triangles) corresponding to $\bar{z}_o = 5$, 10, 15, 20 and 28 km, respectively. Each symbol represents the results of one numerical experiment. Black and gray symbols represent results for strong (flow law 6 [52] in Table 2) and intermediate (flow law 3 [51]) rheologies, respectively. Rift half-width is predicted to increase with decreasing geothermal gradient. Note that smaller geothermal gradients also result in larger changes in rift half-width with increasing crustal thickness.

Table 2
Experimental flow laws for crustal and mantle rocks

Curve	Material	A (MPa^{-1} s^{-1})	n	Q (kJ mol^{-1})	Reference
Weak crust					
1	Heavitree quartzite (wet)	2.91×10^{-3}	1.8	151	[57]
2	Westerly granite (wet)	2.00×10^{-4}	1.9	140	[50]
Intermediate crust					
3	Maryland diabase (wet)	6.12×10^{-2}	3.05	276	[51]
4	Westerly granite (dry)	2.00×10^{-6}	3.3	186	[50]
5	Heavitree quartzite (dry)	5.00×10^{-6}	3.2	220	[58]
Strong crust					
6	Maryland diabase (dry)	1.90×10^{2}	4.7	485	[52]
Mantle					
7	Dunite (dry)	1.00×10^{3}	3	520	[32]

half-width between the mantle- and crust-dominated deformation regimes.

Fig. 9 provides a summary of the combined effects of crustal thickness, crustal rheology and vertical geothermal gradient on rift half-width. In general, when crustal thickness is small and deformation is mantle-dominated, rift half-width is predicted to be controlled primarily by the vertical geothermal gradient. In contrast, when crustal thickness is large and deformation is crust-dominated, the calculated rift half-width is a function of both crustal rheology and vertical geothermal gradient.

4. Discussion

4.1. Strain-rate vs. strain softening

While previous modeling studies have examined the effect of strain softening on strain localization in the lithosphere [29–31], the goal of this study is to investigate strain-rate softening as a mechanism for fault generation in a continuum model. Our choice of weakening mechanisms was motivated by several considerations. First, laboratory studies have shown that frictional strength on fault surfaces is a function of (1) the sliding velocity during periods of steady-state sliding [6,7,35] and (2) the length of the hold time during interseismic periods [36–38]. Furthermore, a recent instability analysis by Montési and Zuber [54] found that velocity weakening on faults results in a highly negative inverse effective stress exponent, indicative of efficient strain localization. Velocity weakening is not the only mechanism characterized by a negative inverse stress exponent. Cohesion loss, shear heating, and grain-size feedbacks are also predicted to produce localization [54]. Poliakov and Buck [29] and Lavier et al. [30] showed that strain softening due to cohesion loss on a fault surface could produce fault-like behavior in numerical models of deformation. In reality, both strain and strain-rate softening are likely to be important mechanisms for strain localization in the lithosphere, and further modeling efforts are necessary to examine the interplay between these processes.

4.2. Crust- vs. mantle-dominated deformation

Most previous studies of normal fault initiation have treated the upper crust as an elastic–plastic layer floating on an inviscid substrate and ignored the effects of a strong upper mantle at depth (e.g., [9–12,14,30]). Results of instability analyses (e.g., [23]) and the numerical calculations presented here, however, clearly suggest that the mantle may play a significant role in controlling deformation in the upper crust, even in the presence of a ductile lower crustal layer. Of particular interest is the thickness of the ductile layer required for transition from mantle-dominated to the crust-dominated deformation. One end-member model that is frequently used to describe this transition proposes that the mere presence of a ductile zone in the lower crust is sufficient to decouple the upper crust from the upper mantle. This model is illustrated by the abrupt transition from mantle- to crust-dominated deformation as a function of crustal thickness predicted by Shaw and Lin [14] (Fig. 6). In contrast, the numerical results presented in this study suggest that rift half-width decreases over a range of crustal thicknesses (Figs. 6 and 9), not at a single, critical value as would be predicted by this end-member model.

Based on the results of our numerical experiments we find that the thickness of the ductile layer required for decoupling is a function of both the vertical geothermal gradient and the crustal rheology (Fig. 9). Specifically, crust-dominated deformation is only predicted when the stress accumulation in the upper crust is much greater than the stress accumulation in the upper mantle. If correct, this implies that deformation in the brittle upper crust will not behave independently of a strong upper mantle, even in the presence of a thick ductile lower crustal channel. This prediction is in agreement with the instability analysis of Zuber et al. [23] and modeling by Braun and Beaumont [26] who found that a strong 'fiber' in the upper mantle could affect the necking style of extending lithosphere. In summary, we conclude that a strong upper mantle will increase the width of active deformation in the upper crust, even in situations where ductile flow occurs in the lower crust.

Table 3
Geophysical parameters for narrow rift zones

Rift zone	Rift basin width (km)	t_c (km)	Heat flow (mW/m^2)	$\frac{\partial T}{\partial z}$ (K/km)
Suez Rift (S)	60–80 [59,60]	~18 [61]	57–86 [62]	17–25
Albert Rift (Al)	40–70 [63,64]	–	28–118 [65]	8–35
Tanganyika Rift (T)	40–70 [63,66]	–	25–110 [67]	7–32
Malawi Rift (M)	50 [68]	–	40–110 [68,69]	12–32
Baikal Rift (B)	50–80 [70,71]	35–46 [72,73]	45–100 [74–76]	13–30
Kenya Rift (K)	60–80 [77,78]	30–40 [79,80]	50–100 [81]	14–30
Ethiopian Rift (E)	30–80 [82]	28–30 [83,84]	75–100 [75]	22–30
Rhine Graben (Rh)	30–40 [85,86]	24–27 [85,87,88]	80–120 [74,89]	23–35
Rio Grande Rift (RG)	~50 [90]	26–30 [91,92]	90–125 [93,74]	26–37
Afar Rift (Af)	3–15 [82]	16–26 [83]	150–250 [75]	44–73
SW Indian Ridge (SWIR)	5–50 [94,95]	2–6 [96,97]	N.A.	50–100
Mid-Atlantic Ridge (MAR)	10–30 [98]	3–8 [99,100]	N.A.	70–150

All references [59–100] are in a **Background Data Set**[1]

4.3. Comparison to natural rifts

A common approach that has been used to explain the development of wide versus narrow rift zones is to integrate the strength of the lithosphere with depth and estimate the force needed for continued extension (e.g., [21,43,45]). If the force decreases with time, extension should stay localized and a narrow rift will form. Alternatively, if the force increases then extension will migrate laterally forming a wide rift. The effects of thermal structure, strain rate, crustal thickness, and lower crustal flow can be incorporated into these models, and the sensitivity of rift style on each of parameter can be assessed [21].

However, while these 1-D models are useful for examining the long-term evolution of extensional systems, they cannot predict the specific pattern of deformation that will be produced by a given set of thermal and rheological conditions. In contrast, the numerical approach presented here allows us to explicitly calculate the preferred location of fault formation for a given set of initial conditions. Fig. 5a illustrates how a wide zone of distributed deformation can develop under laterally homogeneous thermal conditions. In contrast, when a regional temperature gradient is present, extension will focus onto one or two primary normal faults and a narrow rift will form (Fig. 5d). The width of narrow rifts is highly dependent on the specific horizontal thermal conditions of the region. However, if we assume that the bounding faults of most narrow rifts are controlled by a relatively broad thermal gradient, we can test the predictions of our numerical models with observations from natural extensional systems.

Table 3 provides a summary of crustal thickness, heat flow, and rift basin width for both narrow continental and oceanic rift zones. Corre-

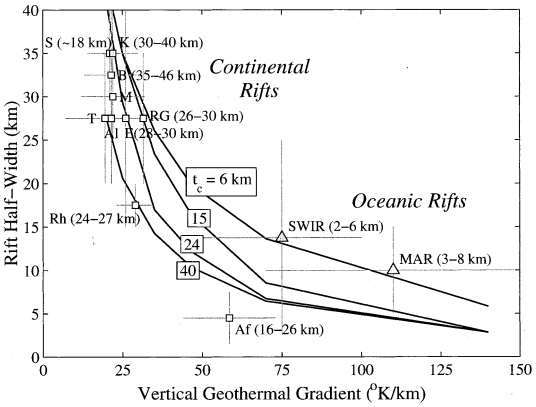

Fig. 10. Predicted rift half-width as a function of vertical geothermal gradient for values of $t_c = 6$, 15, 24 and 40 km (solid lines). Gray squares and triangles show data from the narrow continental and oceanic rifts compiled in Table 3, respectively. Observed crustal thicknesses are given in parentheses. Error bars for data points are shown with gray lines.

[1] http://www.elsevier.com/locate/epsl

sponding vertical geothermal gradients for continental rifts have been calculated from heat flow values after Pollack and Chapman [55]. Because hydrothermal circulation makes heat flow measurements at mid-ocean ridges difficult to interpret, geothermal gradients at the Mid-Atlantic Ridge and Southwest Indian Ridge were calculated from the passive flow model of Phipps Morgan and Forsyth [56]. Rift basin width reflects as closely as possible the average distance separating the main bounding faults of each rift. However, there is significant uncertainty in these estimates as basin width is often highly variable along an individual rift. Furthermore temporal evolution, local magmatism, and fault scarp retreat can all alter the width of the rift basin in ways not accounted for in our model.

In Fig. 10 we compare model predictions of rift half-width with the data for the natural rift zones compiled in Table 3. Predicted rift half-widths are calculated as a function of the vertical geothermal gradient for an intermediate crustal rheology and crustal thickness values of 6, 15, 24 and 40 km, respectively. Acknowledging the uncertainties involved in estimating both basin width and geothermal gradient for natural rift zones, the data clearly show a transition from cool, wide continental rifts to warm, narrow oceanic rifts that is consistent with the predictions of our model. Comparing our results to the elasto-visco-plastic calculations of Chéry et al. [28], we find that for similar rheologic structures our model predicts narrower rifts. This discrepancy is likely related to the fact that we calculate rift width as a function of the distance between the bounding faults. In contrast, because Chéry et al. [28] do not include localization, deformation is more distributed and rift width is calculated from the location of the uplifted rift flanks. Future work will involve more focused studies of individual rifting environments in order to place more quantitative constraints on the thermal and rheologic conditions at depth.

5. Conclusions

The results of this study illustrate how strain-rate softening in the brittle regime affects the pattern of lithospheric deformation in extensional settings. For strain-rate softening coefficients ≥ 0.10, localized zones of high strain-rate are predicted to develop in response to the rheology and boundary conditions. We argue that these narrow shear zones, typically characterized by strain rates four to six orders of magnitude greater than the adjacent regions, are analogous to normal faults. Because these fault-like zones are not imposed a priori, we have used the calculated deformation field to investigate the sensitivity of crustal deformation to thermal state, crustal thickness, and rock rheology.

When no regional temperature gradient is imposed, deformation is predicted to be distributed between several sets of conjugate normal faults. However, in the presence of a horizontally varying temperature field, faulting is predicted to focus where the lithosphere is thinnest. We also investigated the effect of crustal thickness, crustal rheology, and vertical geothermal gradient on rift half-width. Our numerical results predict that when crustal thickness is small, deformation will be mantle-dominated and rift half-width will be controlled primarily by the vertical geothermal gradient. In contrast, when crustal thickness is large and deformation becomes crust-dominated, rift half-width will be a function of both crustal rheology and the vertical geothermal gradient.

We hypothesize that the transition between crust-dominated and mantle-dominated deformation is related to the relative stress accumulation in the upper crust and upper mantle. Model results predict that for the range of parameters examined in this study, crust-dominated deformation will occur only when the stress accumulation in the upper crust becomes much greater than the stress accumulation in the upper mantle. This implies that deformation in the brittle upper crust does not behave independently of a strong upper mantle, even in situations where ductile flow occurs in the lower crust.

Acknowledgements

We thank Jean Chéry and an anonymous re-

viewer for their insightful comments on an earlier version of this manuscript. This work benefited from many constructive discussions with Laurent Montési, Greg Hirth, Brian Tucholke, Jennifer Georgen, and Greg Neumann. Work supported by NASA grants NAG5-9143 and NAG5-11113 (M.T.Z.) and NSF Grant OCE-9811924 (J.L.). WHOI contribution number 10545.*[AC]*

References

[1] W. Brace, D. Kohlstedt, Limits on lithospheric stress imposed by laboratory experiments, J. Geophys. Res. 85 (1980) 6248–6252.
[2] D. Kohlstedt, B. Evans, S. Mackwell, Strength of the lithosphere: Constraints imposed by laboratory experiments, J. Geophys. Res. 100 (1995) 17587–17602.
[3] J. Byerlee, Friction of rocks, Pure Appl. Geophys. 116 (1978) 615–626.
[4] J. Dieterich, Modeling of rock friction 1. Experimental results and constitutive equations, J. Geophys. Res. 84 (1979) 2161–2168.
[5] A. Ruina, Slip instability and state variable friction laws, J. Geophys. Res. 88 (1983) 10359–10370.
[6] E. Rabinowicz, Friction and Wear of Materials, John Wiley, New York, 1965.
[7] C. Scholz, J. Engelder, The role of asperity indentation and ploughing in rock friction: I. Asperity creep and stick slip, Int. J. Rock. Mech. Mining Sci. 13 (1976) 149–154.
[8] S. Kirby, Rheology of the lithosphere, Rev. Geophys. Space Phys. 21 (1983) 1458–1487.
[9] F. Vening Meinesz, Les grabens africains résultant de compression ou de tension dans la croûte terrestre?, Inst. R. Kolon. Belge Bull. 21 (1950) 539–552.
[10] M. Bott, Crustal doming and the mechanism of continental rifting, Tectonophys 73 (1981) 1–8.
[11] D. Forsyth, Finite extension and low-angle normal faulting, Geology 20 (1992) 27–30.
[12] W. Buck, Effect of lithospheric thickness on the formation of high- and low-angle normal faults, Geology 21 (1993) 933–936.
[13] P. Shaw, J. Lin, Causes and consequences of variations in faulting style at the Mid-Atlantic Ridge, J. Geophys. Res. 98 (1993) 21839–21851.
[14] W. Shaw, J. Lin, Models of ocean ridge lithospheric deformation: Dependence on crustal thickness, spreading rate, and segmentation, J. Geophys. Res. 101 (1996) 17977–17993.
[15] H. Melosh, C. Williams, A simple and efficient method for introducing faults into finite element computations, Bull. Seis. Soc. Am. 71 (1981) 1391–1400.
[16] H. Melosh, J. Wiliams, C.A., Mechanics of graben formation in crustal rocks: A finite element analysis, J. Geophys. Res. 94 (1989) 13961–13973.
[17] R. Boutilier, C. Keen, Geodynamic models of fault-controlled extension, Tectonics 13 (1994) 439–454.
[18] J. Chéry, Core complex mechanics: From the Gulf of Corinth to the Snake Range, Geology 29 (2001) 439–442.
[19] M. Zuber, E. Parmentier, Lithospheric necking: A dynamic model for rift morphology, Earth Planet. Sci. Lett. 77 (1986) 373–383.
[20] J. Lin, E. Parmentier, A finite amplitude necking model of rifting in brittle lithosphere, J. Geophys. Res. 95 (1990) 4909–4923.
[21] W. Buck, Modes of continental lithospheric extension, J. Geophys. Res. 96 (1991) 20161–20178.
[22] R. Fletcher, B. Hallet, Unstable extension of the lithosphere: A mechanical model for Basin and Range structure, J. Geophys. Res. 88 (1983) 7457–7466.
[23] M. Zuber, E. Parmentier, R. Fletcher, Extension of continental lithosphere: A model for two scales of Basin and Range deformation, J. Geophys. Res. 91 (1986) 4826–4838.
[24] Y. Chen, W. Morgan, A nonlinear rheology model for mid-ocean ridge axis topography, J. Geophys. Res. 95 (1990) 17583–17604.
[25] J. Braun, C. Beaumont, Styles of continental rifting: Results from dynamic models of lithospheric extension, in: C. geaumont, A. Tankard (Eds.), Sedimentary Basins and Basin-Forming Mechanisms, Vol. Memoir 12, Can. Soc. Petrol. Geol., 1987, pp. 241–258.
[26] J. Braun, C. Beaumont, A physical explanation of the relation between flank uplifts and the breakup unconformity at rifted continental margins, Geology 17 (1989) 76–764.
[27] G. Bassi, Factors controlling the style of continental rifting: insights from numerical modeling, Earth Planet. Sci. Lett. 105 (1991) 430–452.
[28] J. Chéry, F. Lucazeau, M. Daignieres, J.-P. Vilotte, Large uplift of rift flanks: A genetic link with lithospheric rigidity?, Earth Planet. Sci. Lett. 112 (1992) 195–211.
[29] A. Poliakov, W. Buck, Mechanics of stretching elastic-plastic-viscous layers: Applications to slow-spreading mid-ocean ridges, in: W. Buck, P. Delaney, J. Karson, Y. Lagabrielle (Eds.), Faulting and Magmatism at Mid-Ocean Ridges, Geophysical Monograph 106, AGU, Washington, DC, 1998, pp. 305–323.
[30] L. Lavier, W. Buck, A. Poliakov, Factors controlling normal fault offset in an ideal brittle layer, J. Geophys. Res. 105 (2000) 23431–23442.
[31] S. Frederiksen, J. Braun, Numerical modelling of strain localisation during extension of the continental lithosphere, Earth Planet. Sci. Lett. 188 (2001) 241–251.
[32] C. Goetze, The mechanisms of creep in olivine, Philos. Trans. R. Soc. Lond. A 288 (1978) 99–119.
[33] C. Scholz, The Mechanics of Earthquakes and Faulting, Cambridge University Press, New York, 1990.
[34] J. Jaeger, N. Cook, Fundamentals of Rock Mechanics, Chapman and Hall, London, 1979.
[35] T. Tullis, J. Weeks, Constitutive behavior and stability of

frictional sliding of granite, Pure Appl. Geophys. 124 (1986) 383–414.
[36] J. Dieterich, Time-dependent friction in rocks, J. Geophys. Res. 77 (1972) 3690–3697.
[37] N. Beeler, T. Tulis, J. Weeks, The roles of time and displacement in the evolution effect in rock friction, Geophys. Res. Lett. 21 (1994) 1987–1990.
[38] C. Marone, The effect of loading rate on static friction and the rate of fault healing during the earthquake cycle, Nature 391 (1998) 69–72.
[39] G. Neumann, M. Zuber, A continuum approach to the development of normal faults, in: J. Daemen, R. Schultz (Eds.), Proc. 35th US Symposium on Rock Mechanics, Balkema, Lake Tahoe, Nevada, 1995, pp. 191–198.
[40] L. Montési, Localization Instability and Origin of Regularly Spaced Faults in Planetary Lithospheres, Ph.D. Thesis, Massachusetts Institute of Technology, Cambridge, MA (2001).
[41] J. Reddy, An Introduction to the Finite Element Method, McGraw-Hill, New York, 1984.
[42] G. Neumann, D. Forsyth, The paradox of the axial profile: Isostatic compensation along the axis of the Mid-Atlantic Ridge, J. Geophys. Res. 98 (1993) 17891–17910.
[43] P. England, Constraints on extension of continental lithosphere, J. Geophys. Res. 88 (1983) 1145–1152.
[44] N. Kusznir, R. Park, The extensional strength of the continental lithosphere: Its dependence on geothermal gradient, and crustal composition and thickness, in: M. Coward, J. Dewey, P. Hancock (Eds.), Continental Extensional Tectonics, Special Pub. No. 28, Geol. Soc. London, 1987, pp. 35–52.
[45] L. Sonder, P. England, Effects of a temperature-dependent rheology on large-scale continental extension, J. Geophys. Res. 94 (1989) 7603–7619.
[46] W. Buck, L. Lavier, A. Poliakov, How to make a wide rift, Philos. Trans. R. Soc. Lond. A 357 (1999) 671–693.
[47] M. Gerbault, E. Burov, A. Poliakov, M. Daignières, Do faults trigger folding in the lithosphere?, Geophys. Res. Lett. 26 (1999) 271–274.
[48] J. Tullis, R. Yund, Hydrolytic weakening of experimentally deformed Westerly granite and Hale albite rock, J. Struct. Geol. 2 (1980) 439–451.
[49] G. Hirth, J. Escartín, J. Lin, The rheology of the lower oceanic crust: Implications for lithospheric deformation at mid-ocean ridges, in: W. Buck, P. Delaney, J. Karson, Y. Lagabrielle (Eds.), Faulting and Magmatism at Mid-Ocean Ridges, Geophys. Mono. 106, AGU, Washington, DC, 1998, pp. 291–303.
[50] F. Hansen, N. Carter, Semibrittle creep of dry and wet Westerly granite at 1000 MPa, 24th U.S. Symposium on Rock Mechanics, Texas A&M University, College Station, Texas, 1983, pp. 429–447.
[51] Y. Caristan, The transition from high temperature creep to fracture in Maryland diabase, J. Geophys. Res. 87 (1982) 6781–6790.
[52] S. Mackwell, M. Zimmerman, D. Kohlstedt, High-temperature deformation of dry diabase with application to tectonics on Venus, J. Geophys. Res. 103 (1998) 975–984.
[53] E. Rutter, K. Brodie, Rheology of the lower crust, in: D. Fountain, R. Arculus (Eds.), Continental Lower Crust, Dev. Geotecton., Elsevier, New York, 1992, pp. 201–267.
[54] L. Montési, M. Zuber, A unified description of localization for application to large-scale tectonics, J. Geophys. Res. 107 (2002) 10.1029/2001JB000465.
[55] H. Pollack, D. Chapman, On the regional variation of heat flow, geotherms, and lithospheric thickness, Tectonophysics 38 (1977) 279–296.
[56] J. Phipps Morgan, D. Forsyth, Three-dimensional flow and temperature perturbations due to a transform offset: Effects on oceanic crust and upper mantle structure, J. Geophys. Res. 93 (1988) 2955–2966.
[57] O. Jaoul, J. Tullis, A. Kronenberg, The effect of varying water contents on the creep behavior of Heavitree quartzite, J. Geophys. Res. 89 (1984) 4298–4312.
[58] A. Kronenberg, J. Tullis, Flow strength of quartz aggregates: Grain size and pressure effects due to hydrolytic weakening, J. Geophys. Res. 89 (1984) 4281–4297.